

# Mixed Symmetry Nuclear Shell Model

J. P. Draayer,<sup>1</sup> V. G. Gueorguiev,<sup>\*1</sup> Feng Pan,<sup>1,2</sup> and Yanan Luo<sup>1,2,3</sup>

<sup>1</sup>*Department of Physics and Astronomy, Louisiana State University,  
Baton Rouge, LA 70803*

<sup>2</sup>*Department of Physics, Liaoning Normal University,  
Dalian 116029, P. R. China*

<sup>3</sup>*Department of Physics, Nankai University,  
Tianjin 300071, P. R. China*

## Abstract

A mixed-symmetry nuclear shell-model scheme for carrying out calculations in regimes where there is a competition between two or more modes is proposed. A one-dimensional toy model is used to demonstrate the concept. The theory is then applied to  $^{24}\text{Mg}$  and  $^{44}\text{Ti}$ . For lower  $pf$ -shell nuclei such as  $^{44-48}\text{Ti}$  and  $^{48}\text{Cr}$  there is strong  $SU(3)$  symmetry breaking due to the spin-orbit interaction. However, the quadrupole collectivity as measured by  $B(E2)$  transition strengths in the yrast band remain high even though  $SU(3)$  appears to be broken. Some results for the so-called  $X(5)$  symmetry that falls along the  $U(5) \leftrightarrow SU(3)$  leg of the Interacting Boson Model are also considered. The results show that the mixed-symmetry concept is effective, even when strong symmetry breaking occurs.

## 1 The Mixed-Mode Concept

Two dominant and often competing modes characterize the structure of atomic nuclei. One is the single-particle structure that is demonstrated by the

---

<sup>\*</sup>On leave of absence from Institute of Nuclear Research and Nuclear Energy, Bulgarian Academy of Sciences, Sofia 1784, Bulgaria.

validity of the mean-field concept; the other is the many-particle collective behavior that is manifested through nuclear deformation. The spherical shell model is the theory of choice whenever single-particle behavior dominates [1]. When deformation dominates, the Elliott  $SU(3)$  model or its pseudo- $SU(3)$  extension is the natural choice [2]. This duality manifests itself in two dominant components in the nuclear Hamiltonian: respectively, the single-particle term,  $H_0 = \sum_i \varepsilon_i n_i$ , and a collective quadrupole-quadrupole interaction,  $H_{QQ} = Q \cdot Q$ . It follows that a simplified Hamiltonian  $H = \sum_i \varepsilon_i n_i - \chi Q \cdot Q$  has two solvable limits.

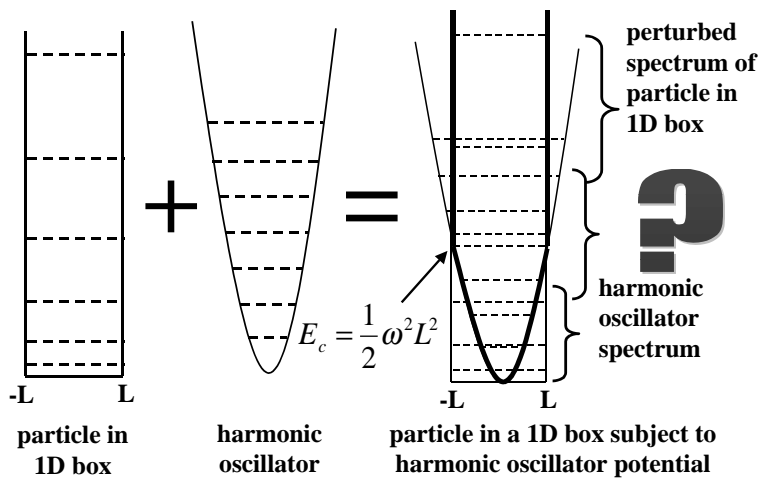


Figure 1: A schematic representation of the potential for a particle in one-dimensional (1D) box at high energies and a harmonic oscillator (HO) restoring force for low energies.

To probe the nature of such a system, one can consider a simpler problem: the one-dimensional harmonic oscillator in a box of size  $2L$  [3]. As for real nuclei, this system has a finite volume and a restoring force of a harmonic oscillator type,  $\omega^2 x^2/2$ . For this model, shown in Figure 1, there is a well-defined energy scale that measures the strength of the potential at the boundary of the box,  $E_c = \omega^2 L^2/2$ . The value of  $E_c$  determines the nature of the low-energy excitations of the system. Specifically, depending on the

value of  $E_c$  there are three spectral types:

- (1) For  $\omega \rightarrow 0$  the spectrum is simply that of a particle in a box;
- (2) At some value of  $\omega$ , the spectrum begins with  $E_c$  followed by the spectrum of a particle in a box perturbed by the harmonic oscillator potential;
- (3) For sufficiently large  $\omega$  the spectrum is that of a harmonic oscillator below  $E_c$  which is followed by the perturbed spectrum of a particle in a box.

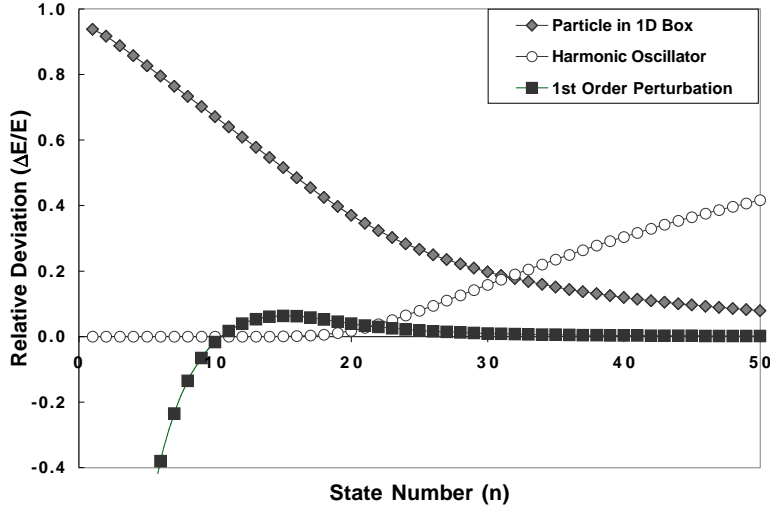


Figure 2: The relative deviations from the exact energy eigenvalues for the 1D box plus HO potential (Figure 1) with  $\omega = 16$ ,  $L = \pi/2$ ,  $\hbar/2\pi = m = 1$ . The open circles represent deviation of the exact energy eigenvalue from the corresponding harmonic-oscillator eigenvalue ( $1 - E_{ho}/E_{exact}$ ), the solid diamonds are the corresponding relative deviation from the energy spectrum of a particle in a 1D box, and the solid squares are the first-order perturbation theory estimates using particle in a 1D box wavefunctions.

The last scenario (3) is the most interesting since it provides an example of a two-mode system. For this case the use of two sets of basis vectors, one representing each of the two limits, has physical appeal, especially at

energies near  $E_c$ . One basis set consists of the harmonic oscillator states; the other set consists of basis states of a particle in a 1D box. We call this combination a mixed-mode / oblique-basis approach. In general, the oblique-basis vectors form a nonorthogonal and overcomplete set. Even though a mixed spectrum is expected around  $E_c$ , our numerical study that includes up to 50 harmonic oscillator states below  $E_c$ , shows that the first order perturbation theory in energy using particle in a 1D box wave functions as the zero order approximation to the exact functions works quite well after the breakdown of the harmonic oscillator like spectrum. This observation is demonstrated in Figure 2 which shows the relative deviations from the exact energy spectrum for a particle in a 1D box.

Although the spectrum seems to be well described using first order perturbation theory based on a particle in a 1D box wave functions, the exact wave functions near  $E_c$  have an interesting structure. For example, the zero order approximation to the wave function used to calculate the energy may not be present at all in the structure of the exact wave function as shown in Figure 3. Another feature also seen in Figure 3 is the common shape of the distribution of the non-zero components along the particle in a 1D box basis. The graph in Figure 4 shows this same effect in nuclei, which is usually attributed to coherent mixing [4, 5].

## 2 Fermion-based Applications of the Theory

An application of the theory to  $^{24}\text{Mg}$  [6], using the realistic two-body interaction of Wildenthal [7], demonstrates the validity of the mixed-mode concept. In this case the oblique-basis consists of the traditional spherical states, that yields a diagonal representation of the single-particle interaction, together with collective  $SU(3)$  configurations, that yields a diagonal representation of the quadrupole-quadrupole interaction. The results shown in Figures 5 and 6 illustrate typical outcomes. For example, a  $\text{SM}(2)+(8,4)\&(9,2)$  model space (third bar in Figure 6) reproduces the binding energy (within 2% of the full-space result) as well as the low-energy spectrum. For this case the calculated eigenstates have greater than 90% overlap with the full-space results. In contrast, for a pure  $m$ -scheme spherical shell-model calculation one needs about 60% of the full space,  $\text{SM}(4)$  – the fourth bar in Figure 6, to obtain comparable results.

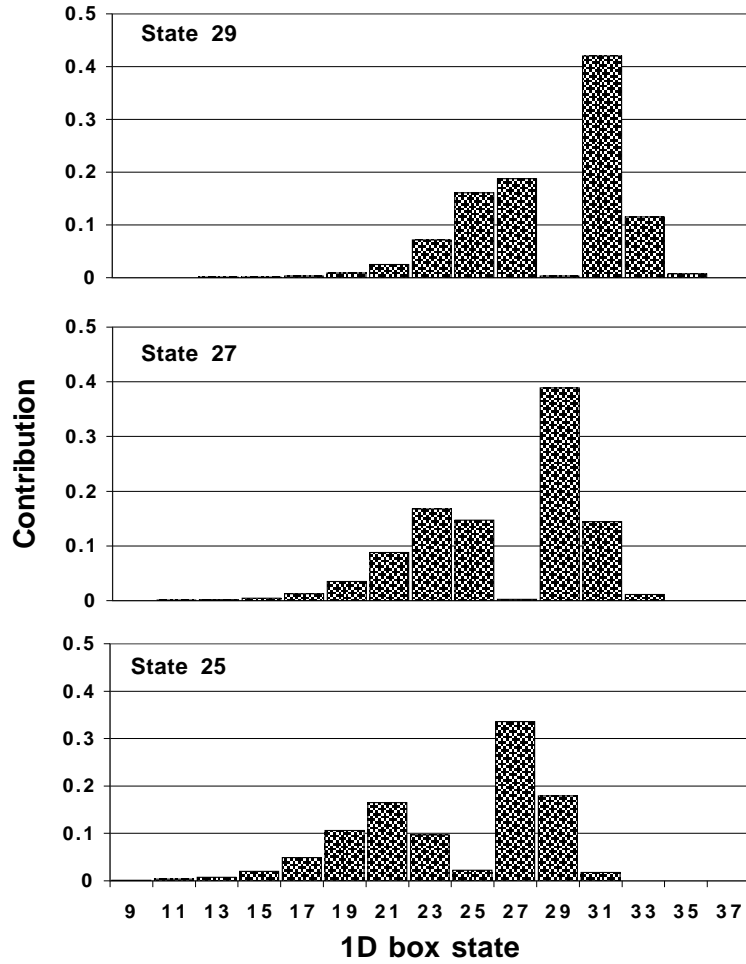


Figure 3: Bar charts that illustrate the similar, coherent structure of the 25th, 27th and 29th exact eigenvectors in the basis of a free particle in a 1D box. Parameters of the Hamiltonian are  $\omega = 16$ ,  $L = \pi/2$ ,  $\hbar/2\pi = m = 1$ .

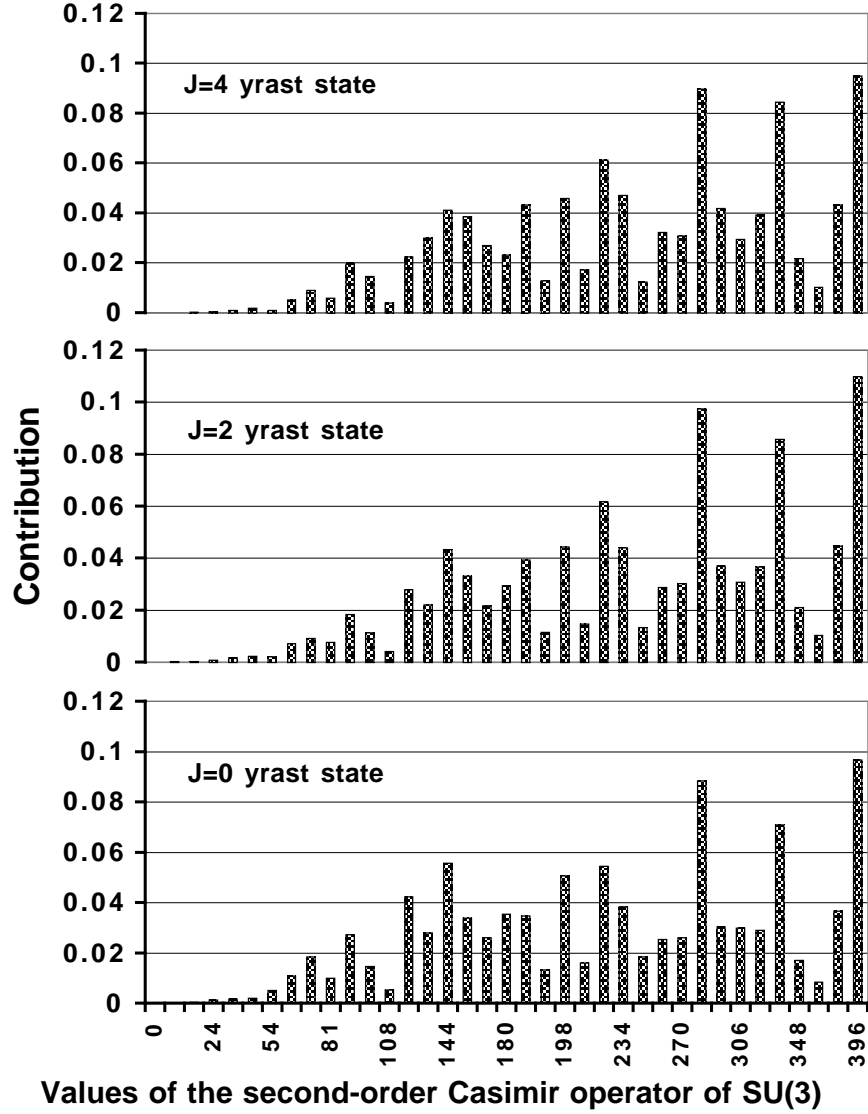


Figure 4: Bar charts that illustrate the very similar, coherent structure of the first three yrast states in  $^{48}\text{Cr}$  calculated using the realistic Kuo-Brown-3 interaction ( $KB3$ ). The horizontal axis is  $C_2$  of  $SU(3)$  while the height of each bar gives the contribution of that configuration to the corresponding yrast state.

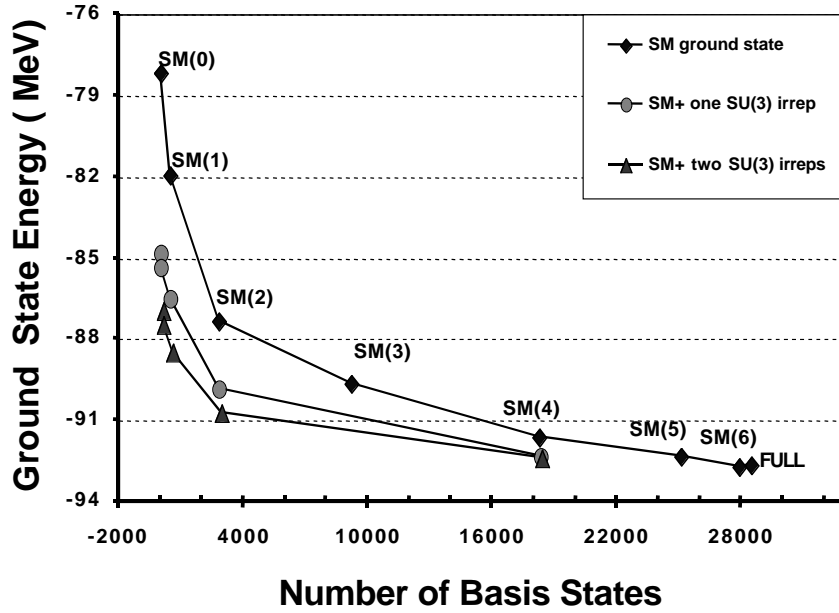
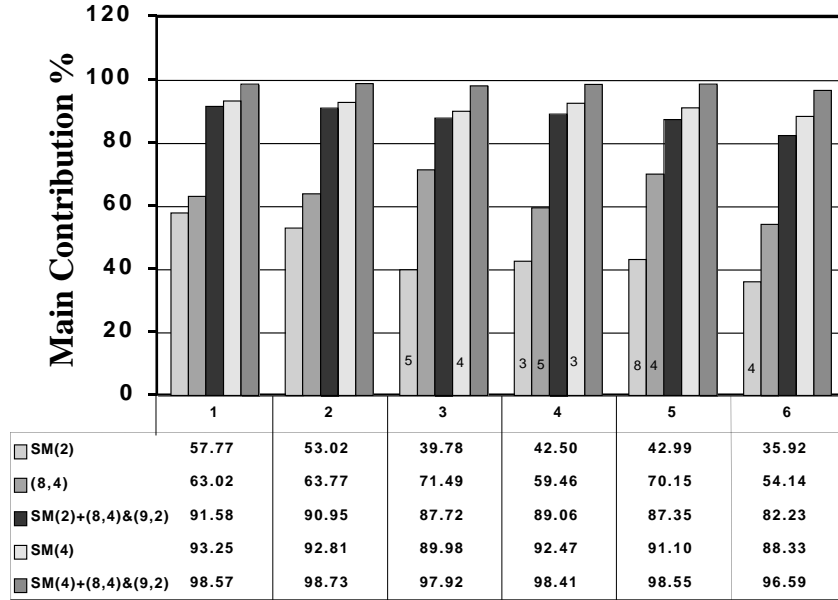


Figure 5: The graph shows the calculated ground-state energy for  $^{24}\text{Mg}$  as a function of various model spaces. SM(n) denotes a spherical shell model calculation with up to n particles outside of the  $d_{5/2}$  sub-shell. Note the dramatic increase in binding (3.3 MeV) in going from SM(2) to SM(2)+(8,4)&(9,2) (a 0.5% increase in the dimensionality of the model space). Enlarging the space from SM(2) to SM(4) (a 54% increase in the dimensionality of the model space) adds 4.2 MeV to the binding energy.



### Eigenvectors

Figure 6: Bar chart that shows representative overlaps of pure  $SM(n)$ , pure  $SU(3)$ , and oblique-basis results with the exact full  $sd$ -shell eigenstates. A number within a bar denotes the state with the overlap shown by the bar if it is different from the number for the exact full-space calculation shown on the abscissa. For example, for  $SM(2)$  the third eigenvector has the largest overlap with the fourth exact eigenstate, not the third, while the fifth  $SM(2)$  eigenvector has greatest overlap with the third exact eigenstate.



Studies of the lower  $pf$ -shell nuclei  $^{44-48}Ti$  and  $^{48}Cr$  [4], using the realistic Kuo-Brown-3 (KB3) interaction [8], show strong  $SU(3)$  symmetry breaking due mainly to the single-particle spin-orbit splitting. Thus the KB3 Hamiltonian could also be considered a two-mode system. This is further supported by the behavior of the yrast band  $B(E2)$  values that seems to be insensitive to fragmentation of the  $SU(3)$  symmetry. Specifically, the quadrupole collectivity as measured by the  $B(E2)$  strengths remains high even though the  $SU(3)$  symmetry is rather badly broken. This has been attributed to a quasi- $SU(3)$  symmetry [5] where the observables behave like a pure  $SU(3)$  symmetry while the true eigenvectors exhibit a strong coherent structure with respect to each of the two bases. This provides justification for further study of the implications of mixed-mode shell-model studies.

Next we discuss oblique-basis type calculations for  $^{44}Ti$  using the KB3 interaction [8]. We confirm that the spherical shell model (SSM) provides a significant part of the low-energy wave functions within a relatively small number of SSMC while a pure  $SU(3)$  shell-model with only few  $SU(3)$  irreps is unsatisfactory. This is the opposite of the situation in the lower  $sd$ -shell. Since the SSM yields relatively good results for SM(2), combining the two basis sets yields even better results with only a very small increase in the overall size of the model space. In particular, results in a SM(2)+ $SU(3)$  model space (47.7% + 2.1% of the full  $pf$ -shell space) are comparable with SM(3) results (84%). Therefore, as for the  $sd$ -shell, combining a few  $SU(3)$  irreps with SM(2) configurations yields excellent results, such as correct spectral structure, lower ground-state energy, and improved structure of the wave functions. However, in the lower  $sd$ -shell  $SU(3)$  is dominant and SSM is recessive (but important) and in the lower  $pf$ -shell one finds the opposite, that is, SSM is dominant and  $SU(3)$  is recessive (but important).

For  $^{44}Ti$  adding the  $SU(3)$  to the SM(2) increases the model space from 47.7% to 49.8% and gives results that are slightly better than the SM(3) which is 84% of the full space. In  $^{24}Mg$  the position of the  $K=2$  band head is correct for the  $SU(3)$ -type calculations but not for the low-dimensional SM(n) calculations [6]. In  $^{44}Ti$  it is the opposite, that is, the SM(n)-type calculations reproduce the position of the  $K=2$  band head while  $SU(3)$ -type calculations cannot. Furthermore, the low-energy levels for the  $SU(3)$  case are higher than for the SM(n) case. Nonetheless, the spectral structure in the oblique-basis calculation is good and the SM(2)+(12,0)&(10,1) spectrum ( $\approx 50\%$  of the full space) is comparable with the SM(3) result (84%).

The overlaps of  $SU(3)$ -type calculated eigenstates with the exact (full shell-model) results are, often less than 40%, but the  $SM(n)$  overlaps are considerably bigger with  $SM(2)$ -type calculations yielding an 80% overlap with the exact states while the results for  $SM(3)$  show overlaps greater than 97%, which is consistent with the fact that  $SM(3)$  covers 84% of the full space. On the other hand,  $SM(2)+(12,0)\&(10,1)$ -type calculations yield results that are as good as those for  $SM(3)$  in only about 50% of the full-space and  $SM(1)+(12,0)\&(10,1)$  overlaps are often bigger than the  $SM(2)$  overlaps. The oblique-bases  $SM(2)+(12,0)\&(10,1)$  results for  $^{44}Ti$  ( $\approx 50\%$ ) yields results that are comparable with the  $SM(3)$  results ( $\approx 84\%$ ). In short, the oblique-basis scheme works well for  $^{44}Ti$ , only in this case, in contrast with the previous results for  $^{24}Mg$  where  $SU(3)$  was found to be dominant and SSM recessive, in the lower  $pf$ -shell SSM is dominant and  $SU(3)$  recessive.

### 3 Boson-based Applications of the Theory

In this section, we consider the transition from the  $U(5)$  vibrational to the  $SU(3)$  rotational limit of the interacting boson model using a schematic Hamiltonian. The behavior of low-lying energy levels and E2 transition rates are studied in detail. The analysis shows that as one moves from the  $SU(3)$  to the  $U(5)$  limit the system transforms from one of maximum deformation to one that is maximally triaxial and soft with the onset of strong triaxiality occurring around the  $X(5)$  critical point.

Understanding shape phase transitions of a finite many-body system is paramount to understanding the system's underlying dynamics. The three possible phases that can occur in the interacting boson model for nuclei have been classified as  $U(5)$ ,  $SU(3)$ , and  $O(6)$  [9]. The  $U(5) \leftrightarrow SU(3)$  transitional description of the rare-earth nuclei Nd, Sm, Gd, and Dy was first reported in [10], including detailed results for most quantities of physical interest. Evidence for coexisting phases at low energy in the spherical-deformed transitional nucleus  $^{152}Sm$  was also analyzed using  $U(5) \leftrightarrow SU(3)$  transitional theory and the results show that the two phases coexist in a very small region of parameter space around the critical point [11]. Recently, since the discovery of the  $X(5)$  symmetry in this region [12], the spherical to axially deformed shape phase transition has attracted further attention [13].

In order to take a close look at the  $U(5) \leftrightarrow SU(3)$  shape phase transition,

we study transitional patterns of many physical quantities, such as low-lying energy levels, isomer shifts, E2 transition rates, and some related quantities across the  $U(5) \leftrightarrow SU(3)$  leg of the Casten triangle. No attempt is made to relate the results to realistic nuclei; rather, our purpose is to gain a better understanding the nature of the  $U(5) \leftrightarrow SU(3)$  transition. In the study, the schematic Hamiltonian

$$\hat{H} = -c \left( x \hat{n}_s + \frac{(1-x)}{f(N)} \hat{Q} \cdot \hat{Q} \right) \quad (1)$$

which has been suggested as a suitable form for describing nuclei in this region is used, where the parameter  $c > 0$ ,  $0 \leq x \leq 1$  is the phase parameter,  $f(N)$  is a linear function of the total number of bosons  $N$ ,  $\hat{n}_s = s^\dagger s$  is the number of  $s$  bosons, and  $\hat{Q} = (s^\dagger \tilde{d} + d^\dagger \tilde{s}) - \frac{\sqrt{7}}{2} (d^\dagger \tilde{d})^{(2)}$ . We note that  $f(N) = 1$  was used in [11], while  $f(N) = 4N$  was adopted in [12] and [14]. Also, the critical point  $x_c$  will be quite different for different choices of the function  $f(N)$ . The Hamiltonian (1) is, up to a constant, equivalent to the one used in [10, 11, 12] and [14] with the relation  $\zeta = 1 - x$ .

In order to diagonalize the Hamiltonian (1), we expand eigenstates of (1) in terms of the  $U(6) \supset SU(3) \supset SO(3)$  basis vectors  $|N(\lambda\mu)KL\rangle$  as

$$|NL_\xi\rangle = \sum_{(\lambda\mu)K} C_{(\lambda\mu)K}^{L\xi} |N(\lambda\mu)KL\rangle, \quad (2)$$

where the quantum number  $\xi$  indicating the  $\xi$ -th level with angular momentum quantum number  $L$  is introduced, and  $C_{(\lambda\mu)K}^{L\xi}$  is the expansion coefficients. Since the total number of bosons  $N$  is fixed for a given nucleus, the above eigenstates will also be denoted as  $|L_\xi; x\rangle$  in the following, in which value of the phase parameter  $x$  is explicitly shown. In our calculation, the orthonormalization process with respect to the band label  $K$  and the phase convention for the  $SU(3) \supset SO(3)$  basis vectors proposed in [15, 16] is used. By using analytic expressions for  $U(6) \supset SU(3)$  reduced matrix element of  $s$ -boson creation or annihilation operator [15] and an algorithm [16, 17] for generating the  $SU(3) \supset SO(3)$  Wigner coefficients, the eigen-equation that simultaneously determines the eigenenergy and the corresponding set of the expansion coefficients  $\{C_{(\lambda\mu)K}^{L\xi}\}$  can be established.

To explore the transitional patterns, we fix the total number of bosons at  $N = 10$  and allow the phase parameter  $x$  to vary in the closed interval  $[0, 1]$ .

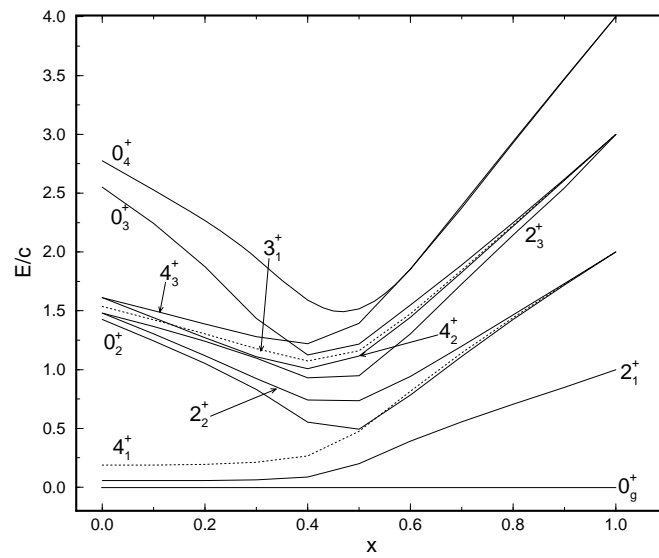


Figure 7: Some low-lying energy levels across the transitional region.

The functional form of  $f(N)$  is chosen to be the same as that used in [12] with  $f(N) = 4N$  unless otherwise specifically noted. Some low-lying energy levels as a function of  $x$  are shown in Figure 7 from which one can see that there is a minimum in the excitation energy around  $x \sim 0.41 - 0.46$ , which corresponds to the spherical-deformed shape coexistence region which is also referred to as the critical (phase transition) region. It can also be seen that the minimum is not exactly the same for all the levels, but all fall within the spherical-deformed shape coexistence region.

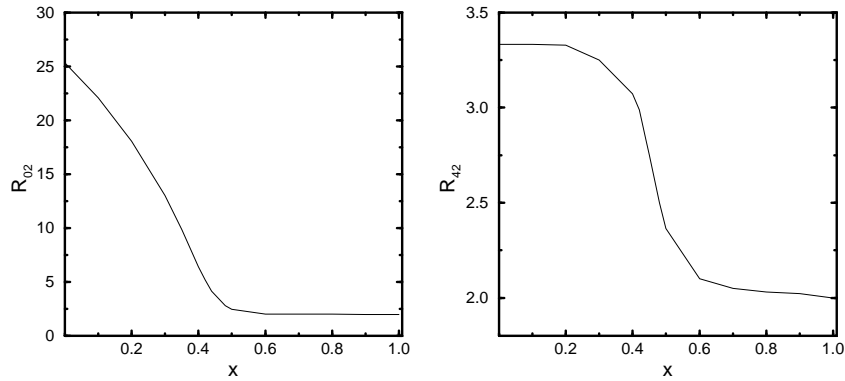


Figure 8: Energy ratios  $R_{02}$  and  $R_{42}$  as functions of the transitional parameter  $x$ .

Two energy ratios,  $R_{02} = E_{0_2^+}/E_{2_1^+}$  and  $R_{42} = E_{4_1^+}/E_{2_1^+}$ , are shown as a function of  $x$  in Figure 8. The ratio  $R_{02}$  drops rather precipitously from the axially deformed limit,  $R_{02} = 25.338$ , to the spherical limit,  $R_{02} \sim 2$ , over the range  $0 \leq x < \sim 0.5$  and then remains at the spherical limit value for  $x > 0.5$ . While the ratio  $R_{42}$  drops rather smoothly as a function of  $x$

from the deformed limit,  $R_{42} = 10/3$  when  $0 \leq x < \sim 0.3$ , to the spherical limit,  $R_{42} = 2$  when  $\sim 0.6 < x \leq 1$ . The sharpest change occurs around the critical point  $x_c \sim 0.46$  when the absolute value of the derivative of  $R_{42}$  with respect to  $x$  reaches the maximal value.

To show how the transition occurs in the ground state, the amplitudes  $|C_{(\lambda\mu)}|^2$  are plotted as functions of  $x$  in Figure 9, which indicate that the most rapid changes in these amplitudes also occur within the coexistence region.

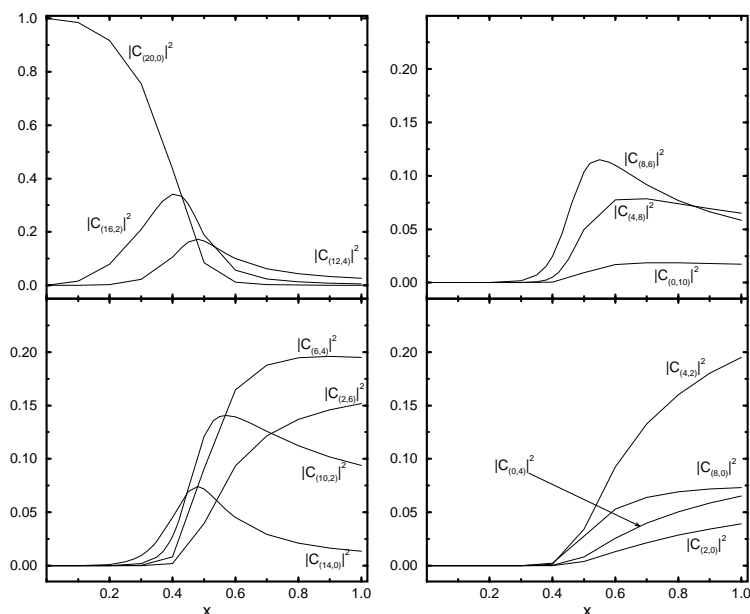


Figure 9: Amplitudes  $|C_{(\lambda\mu)}|^2$  of the ground state as functions of the transitional parameter  $x$ .

In order to explore the exact nature of the critical point with different choices for the linear function  $f(N)$ , overlaps  $|\langle 0_g^+; x | 0_g^+; x_0 \rangle|$  with  $x_0 = 0$  or 1 as suggested in [12] with  $f(N) = 0.5N$ ,  $2N$ ,  $4N$ , and  $8N$ , respectively, were calculated. The results are shown in Figure 10, from which it can be clearly seen that the critical (crossing) point changes with different choices of the function  $f(N)$ . The larger the  $f(N)$  value, the smaller the critical point value  $x_c$ . This conclusion confirms the early result shown in [11], in which the critical point value is very large with  $x_c = 0.974$  corresponding to  $f(N) = 1$ ,

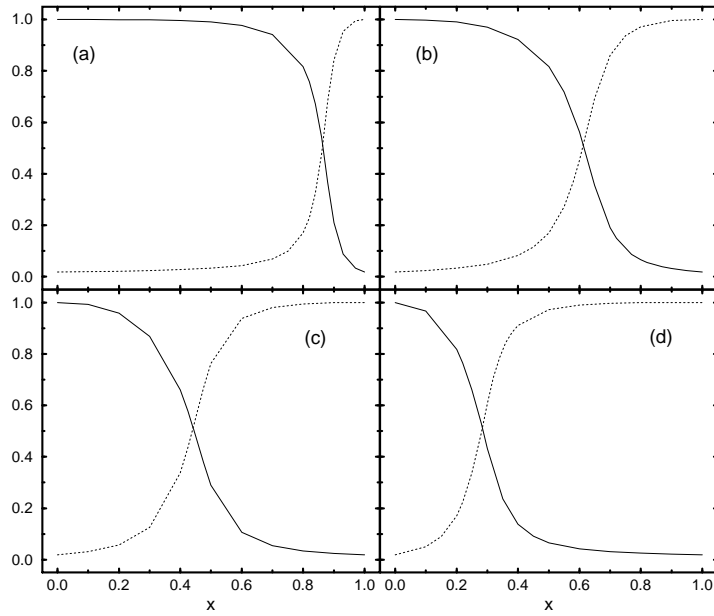


Figure 10: Overlaps of the ground state wavefunction, where the full line shows the overlap  $|\langle 0_g^+; x=0 | 0_g^+; x \rangle|$ , and the dotted line shows the overlap  $|\langle 0_g^+; x=1 | 0_g^+; x \rangle|$ . (a)  $f(N) = 0.5N$ ; (b)  $f(N) = 2N$ ; (c)  $f(N) = 4N$ ; (d)  $f(N) = 8N$ .

while for  $x_c \sim 0.46$  when  $f(N) = 4N$  with  $N = 10$  is used [12, 14]. It should also be pointed out that the critical point may differ from one excited state to the next for the same choice of  $f(N)$ . Our calculation shows that the critical points for  $0_g^+$ ,  $2_1^+$ , and  $4_1^+$  are almost the same, but they are somewhat different for  $2_3^+$  and  $3_1^+$ . It should also be noted that curves of the overlaps  $|\langle L_\xi^+; x | L_\xi^+; x_0 \rangle|$  with  $x_0 = 0$  or  $1$  even become irregular for  $0_2^+$ ,  $2_2^+$ ,  $4_2^+$ , and  $0_3^+$ . Typical examples of these curves for higher excited states are shown in Figure 11, which indicate that the critical point for higher excited states may be quite different from that for ground state. This behavior will be seen in other observables such as E2 transition rates since the critical behavior of the initial and final states may quite different from that of ground state.

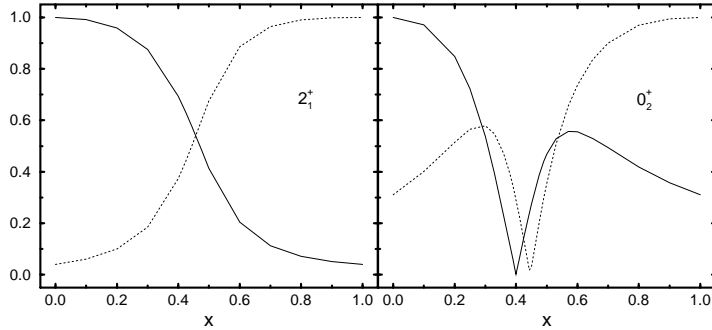


Figure 11: Typical overlaps of two excited states, where the full line shows the overlap  $|\langle L_\xi^+; x = 0 | L_\xi^+; x \rangle|$ , and the dotted line shows the overlap  $|\langle L_\xi^+; x = 1 | L_\xi^+; x \rangle|$ .

Various B(E2) values and ratios among the low-lying levels were studied using the E2 operator is  $T(E2) = q_2 \hat{Q}$ , where  $q_2$  is the effective charge. Some B(E2) values and ratios were found to be sensitive to the shape phase



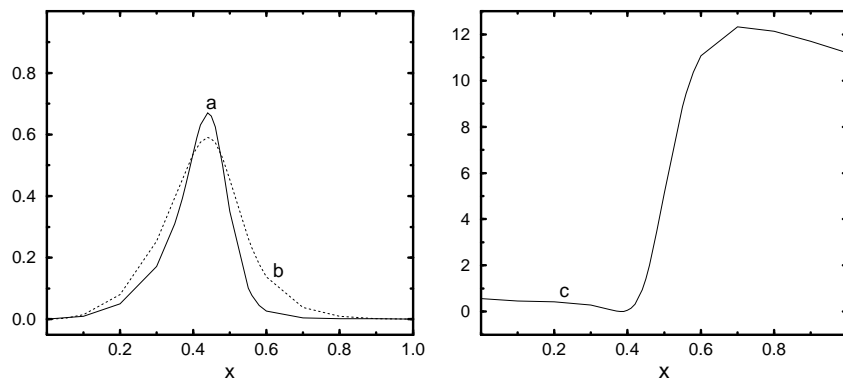


Figure 12: Some  $B(E2)/q_2^2$  values as functions of the transitional parameter  $x$ , where curve a represents  $B(E2, 2_3^+ \rightarrow 0_g^+)/q_2^2$ , curve b represents  $B(E2, 2_3^+ \rightarrow 2_1^+)/q_2^2$ , and curve c represents  $B(E2, 2_3^+ \rightarrow 0_2^+)/q_2^2$ .

transition. Figure 12 provides three B(E2) values,  $B(E2, 2_3^+ \rightarrow 0_g^+)$ ,  $B(E2, 2_3^+ \rightarrow 2_1^+)$ , and  $B(E2, 2_3^+ \rightarrow 0_2^+)$ . There is a small peak around  $x \sim 0.44$  for  $B(E2, 2_3^+ \rightarrow 0_g^+)$  and  $B(E2, 2_3^+ \rightarrow 2_1^+)$ , while there is a saddle point around  $x \sim 0.38$  for  $B(E2, 2_3^+ \rightarrow 0_2^+)$ . As seen previously, the peak and saddle points in these B(E2) values are different from the critical point of the ground state due to different critical behavior of the excited states. Figure 13 provides six B(E2) ratios,  $B(E2; 2_2^+ \rightarrow 0_g^+)/B(E2; 2_2^+ \rightarrow 2_1^+)$ ,  $B(E2; 2_2^+ \rightarrow 2_1^+)/B(E2; 2_1^+ \rightarrow 0_g^+)$ ,  $B(E2; 2_3^+ \rightarrow 0_2^+)/B(E2; 2_1^+ \rightarrow 0_g^+)$ ,  $B(E2; 2_3^+ \rightarrow 0_1^+)/B(E2; 2_3^+ \rightarrow 0_2^+)$ ,  $B(E2; 2_3^+ \rightarrow 2_1^+)/B(E2; 2_3^+ \rightarrow 0_g^+)$ , and  $B(E2; 3_1^+ \rightarrow 2_1^+)/B(E2; 3_1^+ \rightarrow 4_1^+)$ . These ratios all undergo noticeable changes within the coexistence region. The most distinctive signature is shown in  $B(E2; 2_3^+ \rightarrow 0_1^+)/B(E2; 2_3^+ \rightarrow 0_2^+)$ , in which there is a giant peak around  $x \sim 0.38$ .

In order to study shape of nuclei around the critical point, we use the relation between the Bohr variables  $(\beta, \gamma)$  of the collective model and the  $(\lambda, \mu)$  labels that define the irreducible representation of the  $SU(3)$  [18]. In this algebraic approach, the Bohr variables can be expressed as a functional of  $SU(3)$  Casimir operator of the second order  $\hat{\beta} = \beta_0 \sqrt{\hat{C}_2(SU(3)) + 3}$ , and  $\hat{\gamma} = \tan^{-1} \left( \frac{\sqrt{3}(\hat{\mu}+1)}{2\lambda+\hat{\mu}+3} \right)$ , where  $\beta_0$  can be taken as a constant and  $\hat{\lambda}$  and  $\hat{\mu}$  should be regarded as operators, of which the results are usual  $\lambda$  and  $\mu$  values when they are applied onto the basis vector of  $SU(3)$ .

Using these definitions for  $\beta$  and  $\gamma$ , we can calculate expectation values,  $\bar{\beta} = \langle 0_g^+; x | \hat{\beta} | 0_g^+; x \rangle$  and  $\bar{\gamma} = \langle 0_g^+; x | \hat{\gamma} | 0_g^+; x \rangle$  in the ground state, and the corresponding root mean square deviations  $\Delta(\beta)$  and  $\Delta(\gamma)$ . These quantities can be used to display shape uncertainty as a function of  $x$ . It is obvious that  $\Delta(\beta)$  and  $\Delta(\gamma)$  are zero when nucleus is spherically deformed with  $x = 0$  indicating there is a definite shape, while the shape becomes less well defined as  $x$  moves away from zero. The values of  $\Delta(\beta)$  and  $\Delta(\gamma)$  are not small in the spherical limit ( $x = 1$ ) due to the quadrupole vibration being not negligible. It can be seen from Figure 14 that there are also obvious changes in  $\bar{\beta}$  and  $\bar{\gamma}$  in the critical region around  $x \sim 0.46$ . Over the whole range, the magnitude of  $\bar{\gamma}$  change is small. In contrast,  $\Delta(\beta)$  reaches a maximum value around  $x \sim 0.5$  which deviates a little from the critical point  $x_c \sim 0.46$  of the ground state, but is still near the critical region. This distinctive signature shows that nucleus is the softest in the critical region. This fact can help us to understand why there is a saddle region in most excited levels. Since a nucleus in this region is comparatively soft, its shape can be changed easily

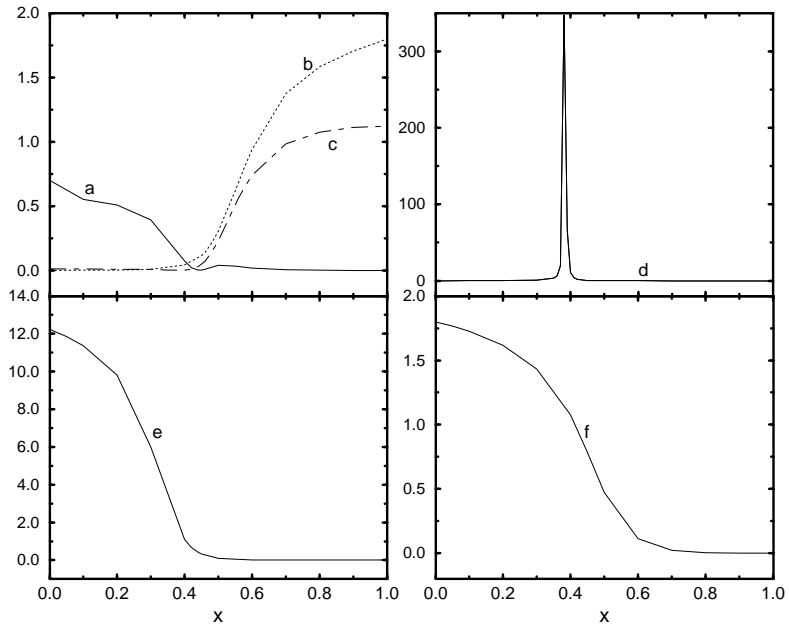


Figure 13: Some B(E2) ratios as functions of the transitional parameter  $x$ , where curve a represents  $B(E2; 2_2^+ \rightarrow 0_g^+) / B(E2; 2_2^+ \rightarrow 2_1^+)$ , curve b represents  $B(E2; 2_2^+ \rightarrow 2_1^+) / B(E2; 2_1^+ \rightarrow 0_g^+)$ , curve c represents  $B(E2; 2_3^+ \rightarrow 0_2^+) / B(E2; 2_1^+ \rightarrow 0_g^+)$ , curve d represents  $B(E2; 2_3^+ \rightarrow 0_1^+) / B(E2; 2_3^+ \rightarrow 0_2^+)$ , curve e represents  $B(E2; 2_3^+ \rightarrow 2_1^+) / B(E2; 2_3^+ \rightarrow 0_g^+)$ , and curve f represents  $B(E2; 3_1^+ \rightarrow 2_1^+) / B(E2; 3_1^+ \rightarrow 4_1^+)$ .

with very little energy. Hence, nuclei in this region can easily be excited, which results in relatively smaller energy gaps in this soft critical region.

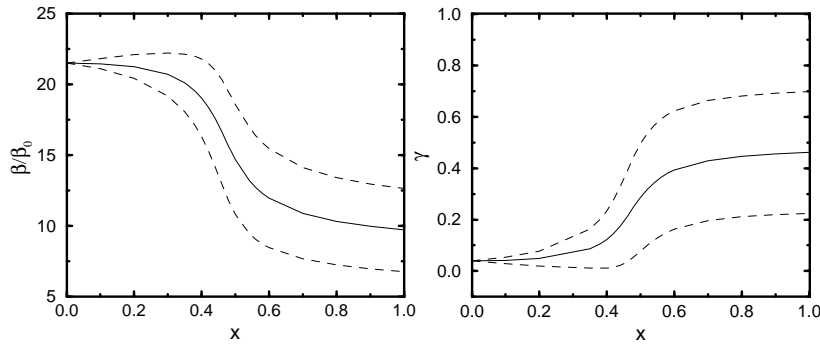


Figure 14: The ground state expectation values of Bohr variables  $\bar{\beta}$  and  $\bar{\gamma}$  and the corresponding root mean square deviations  $\Delta(\beta)$  and  $\Delta(\gamma)$ , where the full line indicates the expectation value  $\bar{\beta}/\beta_0$  or  $\bar{\gamma}$ , while the dotted lines show the corresponding root mean square deviations  $\pm\Delta(\beta)$  or  $\pm\Delta(\gamma)$ .

In summary, transitional patterns from the vibrational,  $U(5)$ , to the rotational,  $SU(3)$ , limit of the interacting boson model with a schematic Hamiltonian have been studied. The transitional behavior of low-lying energy levels, isomer shifts, E2 transition rates, and related quantities over the whole  $U(5) \leftrightarrow SU(3)$  transitional region were explored. The results show that there are many distinctive signatures in the energy levels, wavefunctions, isomer shift, BE2 values and ratios, and expectation value of Bohr variables near the critical point. Generally speaking, critical the behavior of excited states are different from that of ground state, which may lead to different critical

point for some physical quantities that link the two. In comparison with the result shown in [20], a nucleus with  $X(5)$  symmetry can approximately be described by the  $U(5) \leftrightarrow SU(3)$  transitional theory within the critical region. Our analysis also shows that shapes of nucleus in the critical region is not well-defined; that is, a nucleus with  $X(5)$  symmetry is soft.

## 4 Conclusions

Future research may provide justification for an extension of the theory to multi-mode shell-model calculations. For example, an immediate extension of the current scheme could use eigenvectors of the pairing interaction [19] within an  $Sp(4)$  algebraic approach to the nuclear structure [21] in addition to collective  $SU(3)$  configurations and spherical shell model states. Alternatively, Hamiltonian driven basis sets could be considered. For example, the method could use eigenstates of near closed shell nuclei obtained from a full shell-model calculation to form Hamiltonian driven J-pair states for mid-shell nuclei [22]. This would mimic the Interacting Boson Model (IBM) [23] and the so-called broken-pair theory [22]. Likewise, the three exact limits of the IBM [24] can be considered to comprise a three-mode system. Nonetheless, the real benefit of the mixed-mode approach is expected when the spaces encountered are too large to allow for exact calculations.

This work was supported by the U.S. National Science Foundation (0140300) and by the Natural Science Foundation of China (10175031).

## References

- [1] R. R. Whitehead, Nucl. Phys. **A182**, 290 (1972); R. R. Whitehead *et al*, Nuclear Physics **9**, eds. M. Baranger and E. Vogt (Plenum Press, New York, 1977)
- [2] J. P Elliott, Proc. Roy. Soc. A **245**, 128 and 562 (1958); A **272**, 557 (1962); A **302**, 509 (1968)
- [3] V. G. Gueorguiev, Ph.D. Dissertation, Louisiana State University (2002)

- [4] V. G. Gueorguiev, J. P. Draayer, and C. W. Johnson, Phys. Rev. C **63**, 14318 (2001)
- [5] P. Rochford and D. J. Rowe, Phys. Lett. **B210**, 5 (1988); A. P. Zuker *et al*, Phys. Rev. C **52**, R1741 (1995); G. Martinez-Pinedo *et al*, Phys. Rev. C **55**, 187 (1997); D. J. Rowe, C. Bahri, and W. Wijesundera, Phys. Rev. Lett. **80**, 4394 (1998); A. Poves, J. Phys. G **25**, 589 (1999); D. J. Rowe, S. Bartlett, and C. Bahri, Phys. Lett. **B 472**, 227 (2000)
- [6] V. G. Gueorguiev *et al*, Phys. Rev. C **65**, 024314 (2002)
- [7] B. H. Wildenthal, Prog. Part. Nucl. Phys. **11**, 5 (1984)
- [8] T. Kuo and G. E. Brown, Nucl. Phys. **A114**, 241 (1968); A. Poves and A. P. Zuker, Phys. Rep. **70**, 235 (1981)
- [9] A. Arima and F. Iachello, Ann. Phys. (N.Y.) **99**, 253 (1976); Ann. Phys. (N.Y.) **111**, 201 (1978); Ann. Phys. (N.Y.) **123**, 468 (1979); R. F. Casten, in Interacting Bose-Fermi System, ed. F. Iachello (Plenum, 1981)
- [10] O. Scholten, F. Iachello, and A. Arima, Ann. Phys. (NY) **115**, 325 (1978)
- [11] F. Iachello, N. V. Zamfir, and R. F. Casten, Phys. Rev. Lett. **81**, 1191 (1998)
- [12] F. Iachello, Phys. Rev. Lett. **87**, 052502 (2001)
- [13] N. V. Zamfir *et al*, Phys. Rev. C **66**, 021304(R) (2002); E. Garcia-Ramos *et al* nucl-th/0304008
- [14] V. Werner *et al*, Phys. Lett. B **527**, 55 (2002)
- [15] G. Rosensteel, Phys. Rev. C **41**, 730 (1990)
- [16] J. P. Draayer and Y. Akiyama, J. Math. Phys. **14**, 1904 (1973)
- [17] Y. Akiyama and J. P. Draayer, Comput. Phys. Commun. **5**, 405 (1973)
- [18] O. Castaños J. P. Draayer, and Y. Leschber, Z. Phys. A **329**, 33 (1988)

- [19] J. Dukelsky, C. Esebbag, and P. Schuck, Phys. Rev. Lett. **87**, 066403 (2001)
- [20] O. Castaños *et al*, Nucl. Phys. A **524**, 469 (1991)
- [21] K. D. Sviratcheva *et al*, J. Phys. A **34**, 8365 (2001)
- [22] K. L. G. Heyde, *The Nuclear Shell Model*, ed. J. M. Irvine (Springer-Verlag, Berlin Heidelberg, 1990)
- [23] F. Iachello, *The Interacting Boson Model* (Cambridgeshire University Press, New York, 1987)
- [24] M. Moshinsky and Y. F. Smirnov, *The Harmonic Oscillator in Modern Physics, Contemporary Concepts in Physics Volume 9*, ed. H. Feshbach (Harwood Academic Publishing, Amsterdam, 1996)

